



# Reconstructing the structural parameters of a precessing vortex by SPIV and acoustic sensors

I. V. Litvinov<sup>1,2</sup> · D. K. Sharaborin<sup>1</sup> · S. I. Shtork<sup>1</sup>

Received: 7 December 2018 / Revised: 14 July 2019 / Accepted: 16 July 2019 / Published online: 8 August 2019  
© Springer-Verlag GmbH Germany, part of Springer Nature 2019

## Abstract

This paper presents an experimental study of a strongly swirling turbulent flow with the formation of a precessing vortex core (PVC) that emerges at the outlet of a tangential swirler nozzle. The studies were carried out using a stereoscopic particle image velocimetry (SPIV) and two acoustic pressure sensors. An analysis of the velocity fields measured by the proper orthogonal decomposition (POD) showed that the precession motion of the vortex makes a significant contribution (more than 34%) to the turbulence kinetic energy, making it possible to consider the PVC effect as a prominent and convenient object for testing theoretical models describing precessing vortex motion. Estimates of the model parameters of the precessing vortex such as the vortex core radius, vortex precession radius, and vortex intensity based on statistical data obtained from uncorrelated PIV images are presented in the paper. The estimated parameters were compared with the parameters obtained by phase averaging the PIV images, and as a result, three-component velocity distributions were obtained relative to the vortex position. The analysis showed that the precession radius, vortex core size, and vortex circulation are normally distributed. The conditional averaging technique made it possible to determine the structural parameters of the PVC, which was confirmed to be a left-handed helical vortex. Due to the rapid disintegration of the PVC above the nozzle, only a portion of the spiral vortex was observed. Therefore, the helical vortex pitch was estimated in a local sense. Basically, all of the approaches gave similar results for the vortex parameters, providing access to the vortex dynamics. In particular, these cross-checked parameters were used to calculate the precession frequency on the basis of the available helical vortex model. The obtained frequency was found to be in good agreement with the experimentally measured precession frequency, confirming the adequacy of the theory.

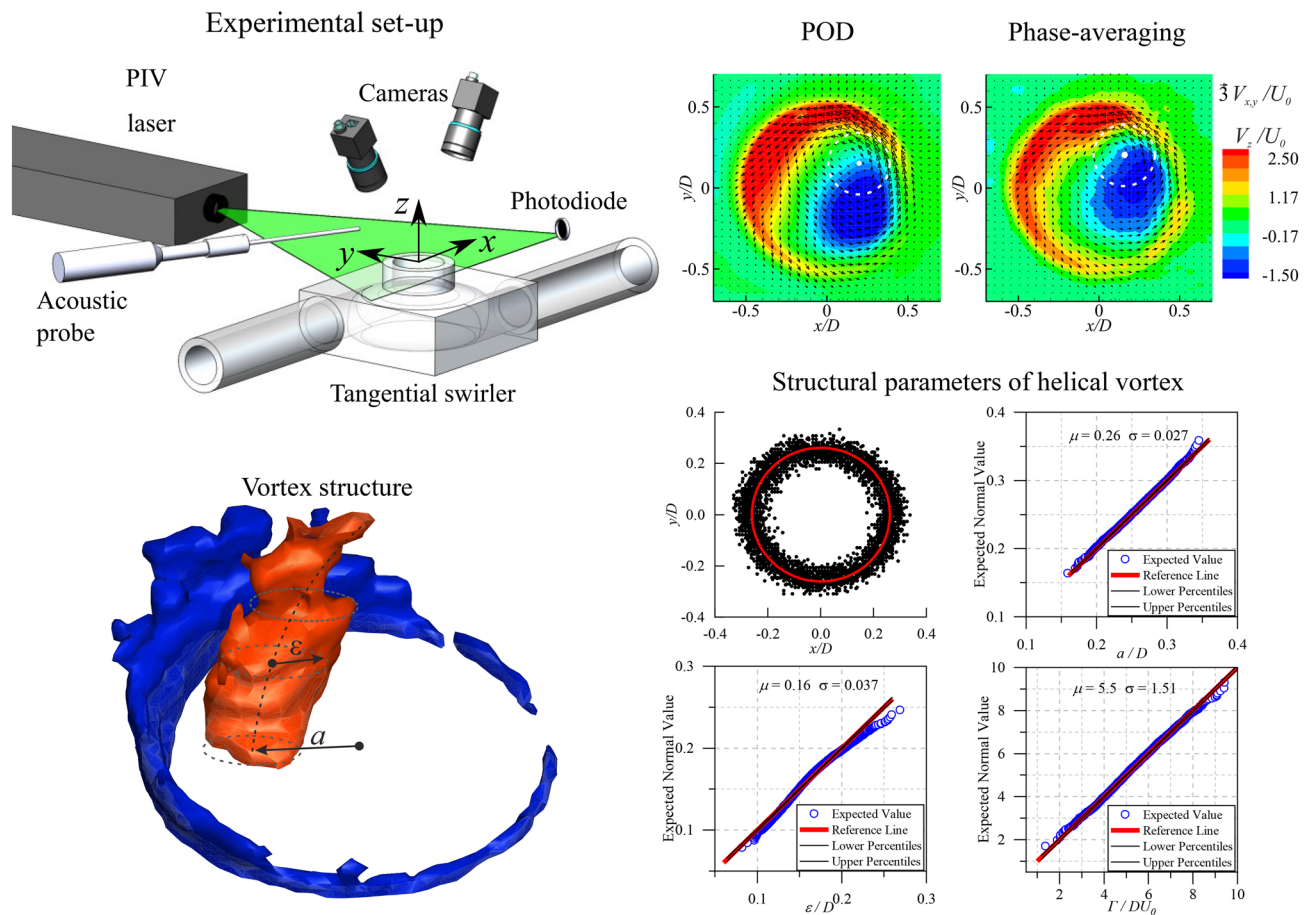
---

✉ I. V. Litvinov  
litvinov@itp.nsc.ru

<sup>1</sup> Kutateladze Institute of Thermophysics SB RAS,  
Novosibirsk, Russia

<sup>2</sup> Novosibirsk State University, Novosibirsk, Russia

## Graphic abstract



## 1 Introduction

High-swirl flows are widely used in various engineering applications, such as fossil fuel burners, cyclone separators, Ranque–Hilsch tubes, vortex diodes, and solar vortex reactors. The main feature of such high-swirl flows is the formation of a region of low pressure and a distinct region of reverse flow. This makes it possible to use swirling flow for particle separation, chemical mixing, combustion, and energy separation. Tangential swirlers are the most common type of swirl generators providing high-swirl numbers compared with those of vane and rotary swirlers (Gupta et al. 1984). In general, a tangential swirler has a simple geometry consisting of just one or a few tangential inlets and an exit nozzle and has no moving parts, which makes it suitable for long-term operation.

The conditions of high-swirl flow and a sudden flow expansion give rise to a vortex phenomenon referred to as a vortex breakdown, leading to dramatic changes in the

flow structure with the formation of an internal shear layer, a stagnation point, and reverse flow usually in the form of a central recirculation zone (CRZ) (Gupta et al. 1984). At high Reynolds numbers and swirl numbers higher than 0.6, the vortex breakdown phenomenon breaks the flow symmetry due to an instability and the establishment of a precessing vortex core (PVC). This phenomenon appears as a quasi-periodic motion of the vortex around the geometric center of the chamber (Syred 2006). We can distinguish the following features in this phenomenon:

- strong flow swirling creates a radial pressure gradient;
- the expansion of the flow causes an axial decay of the tangential velocity, which also contributes to the formation of a radial pressure gradient;
- a negative axial pressure gradient is formed which causes the formation of a central recirculation zone (CRZ);

- the formation of the CRZ and the occurrence of the PVC effect are conjugate phenomena.

The high-swirl flow resulting, as mentioned above, in the formation of a PVC and a CRZ may be useful for enhanced mixing and improved flame stabilization and particle and energy separation. The CRZ formation, often coupled with the PVC effect, is crucial for the stable operation of various devices, such as gas turbines and burners (Gupta et al. 1984; Syred 2006), cyclone separators (Derksen and Van den Akker, 2000), Ranque–Hilsch vortex tubes (Guo and Zhang 2018; Kurosaka 1982; Piralishvili and Polyakov 1996), vortex diodes (Kulkarni et al. 2009; Pandare and Ranade 2015), plasma chambers (Gorbunova et al. 2016; Klimov et al. 2008), and solar vortex particle reactors (Chinnici et al. 2015).

On the other hand, the PVC effect can be considered to be potentially unfavorable and dangerous for engineering applications. Unwanted noise or “cyclone hum” during the operation of cyclone cleaners is a result of the precessing motion of the vortex core and its associated pressure oscillations. In larger industrial units, this can even lead to structural damage (Grimble and Agarwal 2015). For the draft tubes of Francis hydroturbines operating at partial load, the PVC phenomenon (vortex rope) is unambiguously regarded as highly undesirable, since it may lead to a dangerous hydroacoustic resonance (Dörfler et al. 2012; Litvinov et al. 2018). In combustion systems, the PVC can produce powerful vibrations and noise and can also modulate the heat release driving thermoacoustic oscillations (Anacleto et al. 2003; Candel et al. 2014; Shtork et al. 2008; Steinberg et al. 2010; Stöhr et al. 2012). In addition to important practical implications, the PVC phenomenon is associated with a spatially complex and time-dependent swirling flow structure, which presents a challenge for a proper mathematical representation. For example, LDV measurements employing an isothermal vortex burner model have revealed the generation of a set of counter rotating secondary vortices accompanying the motion of the primary PVC structure (Cala et al. 2006). Experimental analysis (Cozzi et al. 2018) has shown that swirl affects the entrainment process in the burner unit in a nontrivial manner. In addition, the PVC has a significant impact on the flame structure due to flame roll-up and flame stretch effects, and a nonlinear interaction with acoustic oscillations has been shown in (Moeck et al. 2012; Stöhr et al. 2012, 2015, 2017a, b). Thus, improving the performance of practical devices utilizing high-swirl flows requires a deeper understanding of the PVC effect and the associated intricate phenomena. Moreover, the PVC phenomenon should be taken into account in the device design stage; the corresponding engineering methods using semiempirical relations or approximate analytical models are in demand, but they are still not reliable enough (Litvinov et al. 2013).

Vortex breakdown as a physical phenomenon has been widely studied for a long time. An overview of different types of vortex breakdown in free and confined flows visualized experimentally can be found in (Alekseenko et al. 2007; Benjamin 1962; Falser and Leibovich 1978; Gupta et al. 1984; Lucca-Negro and O’Doherty 2001). As shown in early papers devoted to the experimental study of the PVC (Cassidy and Falvey 1969; Chanaud 1965), the precession frequency is a linear function of the flow rate. In addition, flow visualization has shown that the precessing vortex has a helical structure. The vortex has a left-handed spiral (helical) vortex structure with its axis spiraling in the direction opposite to the direction of the flow swirl. The helical structure starts to precess due to the effect of self-induced motion generating a reverse flow along the chamber axis (Alekseenko et al. 1999). Based on previous studies (Garg and Leibovich, 1979; Gupta et al. 1984; Liang and Maxworthy, 2005; Lucca-Negro and O’Doherty, 2001; Markovich et al. 2016; Oberleithner et al. 2012, 2011; Smith et al. 2018; Syred, 2006), the positive helical mode  $m = 1$  (left-handed single helix) of the instability arising from the vortex breakdown is identified in different swirl flows for sufficiently high-swirl numbers and Reynolds numbers.

The PVC is generally associated with the presence of distinct peaks in the power spectrum of the pressure and velocity fluctuations. The coherent fluctuations associated with the vortex precession induce a high fluctuation intensity close to the vortex core. The problem of distinguishing the coherent contribution of the PVC from the overall turbulence level was considered in a number of papers (Grosjean et al. 1997 among others). The authors of the cited study carried out a comparative analysis of the PVC using LDA and PIV systems. The effect of the PVC on the probability density function (PDF) of the velocity pulsations at various points of the velocity profile in a nonstationary swirling flow was discussed in (Martinelli et al. 2007; Wunenburger et al. 1999). The authors noted that the empirical data strongly deviated from a Gaussian distribution.

Since the PVC effect produces a strictly periodic signal in time, in some studies (Cala et al. 2006; Martinelli et al. 2012; Valera-Medina et al. 2009; Yazdabadi et al. 1994; Zakharov et al. 2014), velocity distributions related to the vortex phase were obtained using a reference signal from a pressure sensor (microphone). As a result, the phase-averaged spatial structure of the PVC was obtained.

As an alternative approach to distinguish a large-scaled coherent structure such as the PVC in a turbulent flow field, Graftieux et al. (2001) employed proper orthogonal decomposition (POD). An analysis of the PIV data showed that two spatial modes are responsible for the PVC coherent motion. The authors proposed using two novel vortex identification functions,  $\Gamma_1$  and  $\Gamma_2$ . These functions identify the locations of the center and boundary of the vortex

on the basis of the velocity field. It was also suggested that this method could be used to separate pseudofluctuations due to the unsteady nature of large-scale vortices from fluctuations due to small-scale turbulence. Later, Stöhr et al. (2011) performed a comparative analysis of velocity fields using POD and phase-locking by averaging with the aid of a reference signal, confirming that the two methods are equivalent. It has been proven that POD analysis can identify periodic structures in the flow and obtain the underlying stochastic turbulence field in confined and free-swirl jets under reaction and isothermal conditions (Ahmed and Birouk 2018; Gomez-Ramirez et al. 2017; Mak and Balabani 2007; Oberleithner et al. 2011; Vanierschot et al. 2014). This approach has been further developed to perform the spectral POD (SPOD) (Sieber et al. 2016b). SPOD combines pure POD and a Fourier decomposition, benefitting from the advantages of both methods. This approach uses a filtered correlation matrix, which allows a clearer identification of coherent structures, as was demonstrated for the flow in a swirl-stabilized combustor (Sieber et al. 2016a). In addition, dynamic mode decomposition (DMD) was employed to describe the unsteady vortex dynamics in swirl flows (Markovich et al. 2014; Towne et al. 2018; Zhang et al. 2019). The extensive use of advanced high-speed PIV and Tomo-PIV has led to significant progress in understanding the PVC phenomena and has provided information about the 3D vortex structure alignment in space and time (Alekseenko et al. 2018; Markovich et al. 2016; Percin et al. 2017).

In general, analytical methods for the study of this subject are not sufficiently developed. An exception is a powerful tool based on linear stability analysis (LSA), which has gained significant attention in the last decade. This analytical assay has been shown to provide a highly accurate prediction of the dominant flow dynamics for the mean turbulent flow under isothermal conditions (Oberleithner et al. 2014) and in swirl flames (Stöhr et al. 2017a, b), although the assay requires a good theoretical background and is often not easily applicable to engineering devices. Nevertheless, the simplification of PVC modeling even for simplified swirl flows is still in demand. Basically, an analytical model has a certain advantage, since it does not require significant computational resources, but makes it possible to estimate the amplitude–frequency characteristics of the turbulent swirling flow. However, the testing and verification of theoretical models require detailed experimental data to select the necessary parameters for the application of the model. It has been shown, e.g., in (Litvinov et al. 2013) that an analytical model of a helical vortex (Alekseenko et al. 1999) can be used to describe the PVC in the near field and a tangential swirler for a range of swirl numbers  $S = 1.4\text{--}2.4$  and  $Re \approx 15,000\text{--}38,000$ . It has been confirmed that the analytical model can be used to identify the PVC and estimate the

structural parameters solely from the time-mean axial and tangential velocities.

In this paper, we present a novel approach to estimate the PVC parameters in a high-swirl flow ( $S = 1.4\text{--}2.4$ ,  $Re = 2 \times 10^4\text{--}4 \times 10^4$ ) directly from experimental data acquired using standard SPIV with conditional averaging over the precession phase and two acoustic sensors. The relationship between the Strouhal number and the Reynolds number shows that at high  $Re$ , the Strouhal number  $Sh$  is independent of the Reynolds number, as stated previously (Syred 2006). The power-law relationship between the Strouhal number and the swirl number was also reported in the literature (Grimble and Agarwal 2015; Litvinov et al. 2013). For this reason, the detailed analysis in the present study is limited to reference experimental conditions with  $S = 2.4$  and  $Re = 2.3 \times 10^4$ . We compare phase-averaging methods with the reconstruction method using the first two most energetic POD modes and analyze all the PIV statistics based on scalar functions as proposed by (Graftieaux et al. 2001). Then, the obtained vortex structure parameters are applied to calculate the precession frequency using an analytical formula derived from the helical vortex model.

## 2 Research methods

### 2.1 Parameter space for a swirl flow

Let us determine the parameters of swirling inhomogeneous incompressible flows. If, based on the work (Grimble and Agarwal 2015), we represent the vortex as a perfectly rigid body with angular rotation frequency  $\Omega$ , linear size of the vortex  $D_v$ , linear size of the region  $L$ , velocity scale  $U$ , and time scale  $\Omega^{-1}$ , and the vorticity equation in dimensionless form is written as follows:

$$\frac{\partial \hat{\omega}}{\partial t} + \frac{1}{S} \left( \hat{u} \cdot \hat{\nabla} \hat{\omega} - \hat{\omega} \cdot \hat{\nabla} \hat{u} \right) = \frac{1}{Re \cdot S} \hat{\nabla}^2 \hat{\omega}, \quad (1)$$

where  $\hat{\cdot}$  denotes a dimensionless quantity,  $\vec{u}$  is the velocity vector at a point,  $\vec{\omega} = \nabla \times \vec{u}$  is the vorticity vector, and  $\nu$  is the kinematic viscosity. In Eq. (1), there are two dimensionless parameters: the Reynolds number  $Re = \frac{UD_v}{\nu}$ , which determines the contribution of viscosity effects to the total balance in the flow scale considered, and the swirl parameter  $S = \frac{\Omega D_v}{U}$ , which characterizes the ratio of the tangential and axial components of the motion of the medium. Often, mean-flow integral parameters are introduced in the literature. In this case, the Reynolds number is defined as  $Re = U_0 D / \nu$ , where  $U_0$  is the bulk velocity,  $D$  is the vortex chamber diameter,  $\nu$  is the kinematic viscosity of the medium (Alekseenko et al. 2007; Cassidy and Falvey 1969; Chanaud 1965; Gupta et al. 1984), and the swirl parameter



is transformed to the form  $S_{int} = \frac{2G_{zz}}{D \cdot G_z}$ . In practice, when the pressure and turbulent pulsations are often neglected,  $G_{zz} = 2\pi\rho \int_0^\infty V_{ax} V_{tg} r^2 dr$  is the flux of angular momentum in the axial direction of the flow,  $G_z = 2\pi\rho \int_0^\infty V_{ax}^2 r dr$  is the momentum flux in the axial direction of the flow, and  $V_{ax}$  and  $V_{tg}$  are the axial and tangential velocity components. The swirl number  $S$  remains a parameter that determines the structure of the swirling flow. However, as noted in a number of works (Alekseenko et al. 1999; Skripkin et al. 2016), these criteria do not always uniquely define the geometry of the vortex flow, since different vortex structures with the same swirl parameters can be observed. The solution of this problem requires the introduction of additional geometric parameters, which will be discussed below.

### 2.2 Helical vortex model

The theoretical approach used in this work is based on the theory of helical vortices. The most complete and detailed information on the theory of helical vortex motion with an analysis of the influence of various factors can be found in (Alekseenko et al. 2007, 1999; Kuibin and Okulov 1998). The initially introduced parameters are determined for a thin vortex filament in an ideal fluid with a uniform vorticity distribution inside the core and vorticity-free flow outside. The starting point for the analytical model of an ideal helical vortex is the direct relationship between the tangential and axial fluid velocity components:

$$V_{ax} = u_{ax} - \frac{2\pi r \cdot V_{tang}}{h}, \tag{2}$$

where  $V_{ax}$  and  $V_{tang}$  are the (mean) axial and tangential velocities,  $u_{ax}$  is the axial velocity at  $r=0$ ,  $h$  is the helical pitch, and  $r$  is the radial coordinate. Equation (2) is in fact an exact solution of the Euler equations for an inviscid fluid, where the flow exhibits helical symmetry, i.e., any function obeys the transformation  $f(r, \theta, z) = f(r, \theta - 2\pi z/h, 0)$ . In real flows, the condition of helical symmetry along the entire length of the axis is not exactly satisfied. In particular, in swirling jets, the flow changes significantly with the distance from the swirler: from the vortex breakdown to the complete decay of the swirl. The assumption of helical symmetry in the proposed model implies a periodic flow structure with the periodicity along the axis on its infinite length. This is a strong restriction, but according to (Alekseenko et al. 2007), swirling flows may have extensive regions (up to several diameters) where the velocity profiles change insignificantly. Therefore, this model allows an estimation of the frequency and amplitude of pressure pulsations generated

by the precessing vortex core in flows in practical devices (Alekseenko et al. 2007; Litvinov et al. 2013, 2015).

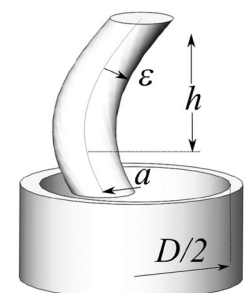
To introduce the model of the helical vortex structure, we should consider the following parameters: the vortex core radius  $\epsilon$ , the radius of the helical structure or the precession radius  $a$ , the tube radius  $D/2$ , the vortex intensity or circulation  $\Gamma$ , the helical pitch  $h$ , and the axial velocity along the flow axis  $u_{ax}$  (see Fig. 1). The formula for estimating the PVC frequency derived for the helical vortex model accounting for all contributions is given in the “Appendix”.

It should be noted that the helical vortex model has been used previously (Litvinov et al. 2013) to describe the near field of a tangential swirler, where the required parameters were determined from the mean velocity profiles using a vortex model with a finite core and a least-squares algorithm. A limitation of the above-mentioned studies is that the obtained velocity profiles were measured using LDA along only one direction in the vertical plane. This means that structural parameters such as  $\epsilon$  and  $a$  can only be indirectly extracted from these data. In the present work, the parameters required for the model are directly determined using an SPIV experiment for different cross-flow sections. To access the spatial structure of the PVC, we use the classic method of phase averaging. These results are additionally cross-checked by a comparison with the results of processing the statistical procedure based on an analysis of uncorrelated PIV images.

### 2.3 Experimental setup

The experiments were carried out in the tangential vortex chamber used in (Litvinov et al. 2013). The design swirl parameter was determined according to (Syred 2006) using the formula  $S = \pi D D_0 / (4A_T)$ , where  $D$  and  $D_0 = 145$  mm are the diameters of the outlet nozzle and the main part of the cyclone chamber, respectively, and  $A_T$  is the area of the tangential inlet nozzles with a diameter of 40 mm. The experiments were carried out for nozzles with diameters of  $D = 30, 40,$  and  $52$  mm at an airflow rate of 15 l/s and a bulk velocity in the nozzle  $U_0$  of 7.06 m/s. As has been shown previously (Gupta et al. 1984; Litvinov et al. 2013; Valera-Medina et al. 2009), the PVC parameters do not depend on

Fig. 1 Schematic diagram of the helical precessing vortex formed in the tube



the flow regime, i.e., self-similarity arises. Therefore, in the present experiments,  $Re$  was fixed ( $Re = 2.3 \times 10^4$ ).

For these nozzles, the design swirl parameters were 1.4, 1.8, and 2.4, and the integral swirl parameter  $S_{int}$  determined from the average velocity profiles were 0.9, 1.07, and 1.31, indicating that for such high values of the swirl parameter, the geometric and integral determinations are not correlated.

## 2.4 Stereo-PIV experiment and phase averaging

To measure the instantaneous velocity fields, we used the POLIS SPIV system consisting of a dual Nd:YAG pulsed laser (70 mJ in a 10-ns pulse), two ImperX CCD cameras (2060 × 2056 pixels, 8 bits), and a synchronizing processor. To form a laser sheet, focusing (spherical) and cylindrical lenses were used. The 1-mm-thick laser sheet was placed in the  $x$ - $y$  plane. The horizontal measurement cross-section  $z = 0.01D$  was located 0.5 mm from the nozzle edge (Fig. 2a). The flow was seeded with 1–3  $\mu\text{m}$  paraffin oil particles generated using the Laskin nozzle method. The cameras of the SPIV system were located at an angle of  $\pm 30^\circ$  relative to the normal of the measurement plane. The cameras were mounted on special swivel brackets with lenses that allowed us to combine the plane of the best focusing camera (located parallel to its matrix) with the laser sheet plane and, thus, perform a Scheimpflug correction (Prasad and Jensen, 1995). The optical system was calibrated using a flat three-level calibration target of 100 × 100 mm with round-shaped support points on a Cartesian grid with a step of 5 mm. To improve the measurement accuracy, we applied an algorithm to correct the possible misalignment of the target and the measurement plane. For each cross-section, 5000 image pairs were captured and processed by a standard iterative cross-correlation algorithm (continuous window shift (CWS) with an image deformation). The uncertainty of the algorithm could be estimated as  $10^{-2}$  px (Scarano 2002). The final interrogation area was  $32 \times 32$  pixels with 50% overlap (final vector spacing of 1.6 mm). The delay between a pair of flashes was 25  $\mu\text{s}$ , and the frequency of the laser flashes was 1.4 Hz. The PVC frequency

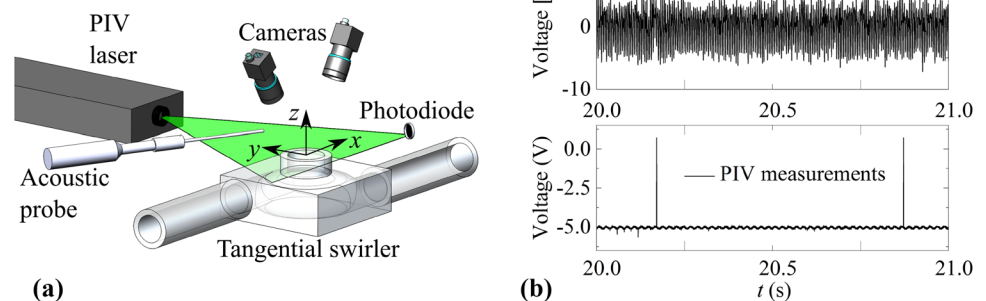
in the experiment was approximately 210 Hz for the case of  $S = 2.4$  and  $U_0 = 7.06$  m/s, which allowed us to collect statistics for 5000 uncorrelated images for each cross-section in approximately one hour. Conditional (phase) averaging was carried out with the help of an analog–digital converter (ADC), which interrogated two channels with a frequency of 10 kHz: the photodiode signal was fed to the first channel, and the signal of the pressure pulsations received from the microphone was fed to the second channel. The signal from the photodiode made it possible to detect the flashes of the laser sheet and determine the instants corresponding to the measurements of velocity distributions (see Fig. 2b). The signal from the microphone was a reference signal that tracked the phase of the vortex core precession. Thus, an unambiguous relationship between the time of the PIV images and the phase of the vortex structure motion was provided. Phase-averaging was normally performed with a vortex phase uncertainty of  $\Delta\theta = \pm 8^\circ$  (approximately 90 PIV images). In the experiments, the measurement cross-section  $z = 0.01$ – $0.5 D$  was varied by moving the tangential swirler and the acoustic sensor along the  $z$  axis by means of a manual traverse device, while the optical configuration of the PIV system remained fixed in space.

## 2.5 Acoustic measurements

In the experiments, the presence of the PVC at the exit of the tangential vortex chamber was confirmed not only by spectral analysis of the signal of the pressure pulsations, but also by the presence of a clearly audible sound tone, which is a consequence of the PVC (Chanaud 1965; Zakharov et al. 2014).

The localized vorticity inside the vortex produces a region of low static pressure, which, together with the precessing motion, generates intense pressure pulsations with a dominant frequency coinciding with that of the velocity fluctuations (Shtork et al. 2008). To detect the pressure pulsations, i.e., the position of the PVC during the PIV experiment, an acoustic sensor based on a Behringer ECM 8000 microphone connected to a thin tip was used as a high-frequency

**Fig. 2** Diagram of the SPIV experiment with conditional averaging



filter (Fig. 2a). The microphone is relatively large and, as a result, can significantly affect the flow pattern. Therefore, the use of a small static pressure receiver allows an increase in the signal-to-noise ratio in local measurements of the pressure pulsations in the flow. To consider the influence of the receiver, the microphone amplitude–frequency characteristics were corrected as outlined in (Litvinov et al. 2013; Shtork et al. 2008).

It is known that at sufficiently high  $Re$  numbers, the non-dimensional PVC frequency is expressed in terms of the Strouhal number  $Sh = f \cdot D/U_0$ , where  $f$  is the PVC frequency in Hz. A typical spectrum of the pressure pulsations in the far field of the jet is shown in Fig. 3a. The dimensionless frequency plotted along the abscissa axis is the Strouhal number. The spectrum clearly shows a peak at a frequency of  $Sh_1 = 1.56$ , which is associated with the frequency of the vortex motion near the acoustic sensor. The successive peaks at  $Sh_2 = 3.11$  and  $Sh_3 = 4.66$  are related to the second and third harmonics, respectively.

The Strouhal number is a nearly constant function of the  $Re$  number, as shown in Fig. 3b. We show, however, that the scaling of the  $Sh$  number with the geometrical swirl number  $S$  leads to similar  $Sh/S$  values for  $S = 1.4$  and 1.8, and 2.4 ( $D = 30, 40,$  and 52 mm). As shown in the literature (Gupta

et al. 1984; Litvinov et al. 2013; Valera-Medina et al. 2009), the PVC parameters do not depend on the flow regime; i.e., self-similarity takes place. A generalization of the PVC frequency in the form of the dependence of the Strouhal number on the swirl number  $S$  for cyclone-like vortex chambers can be found in (Grimble and Agarwal 2015; Syred 2006). This, in particular, justifies limiting the procedure of the present study to a single experimental condition (nozzle diameter  $D = 52$  mm,  $S = 2.4$ , and one fixed  $Re$ ).

To obtain phase-averaged pressure distributions, we employed a special technique that has already been used for this flow (Litvinov et al. 2013). Two acoustic sensors based on an ECM8000 Behringer microphone and 2250 Type B&K with attached tips were placed opposite to each other on the nozzle edge of the tangential vortex chamber. The ECM8000 Behringer sensor was fixed (reference sensor), and the 2250 Type B&K sensor (primary sensor) was moved along the  $x$ - and  $z$ -axes from the nozzle center to its edge with steps of 1 mm and 2–10 mm, respectively, using an automated axis controller (Fig. 4a). The signals from both probes were recorded with an ADC board for 30 s with an acquisition frequency of 4 kHz. Phase-averaging was normally performed with a vortex phase uncertainty of  $\Delta\theta = \pm 19^\circ$ . It should be noted that the uncertainty of the

**Fig. 3** Typical power spectral density of the pressure pulsations in the far field of a tangential swirler ( $D = 52$  mm,  $S = 2.4$ ,  $Q = 15$  l/s, and  $Re = 2.3 \cdot 10^4$ ) (a); Strouhal number divided by  $S$  as a function of  $Re$  for three different nozzle diameters ( $S = 1.4, 1.8,$  and 2.4;  $D = 30, 40,$  and 52 mm, respectively) (b)

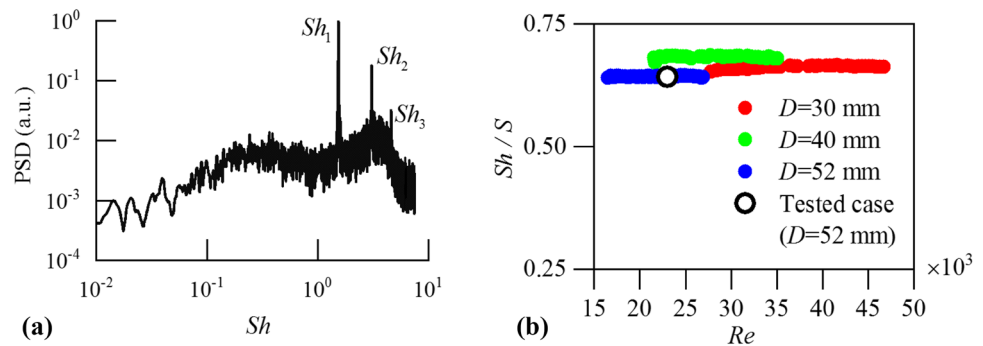
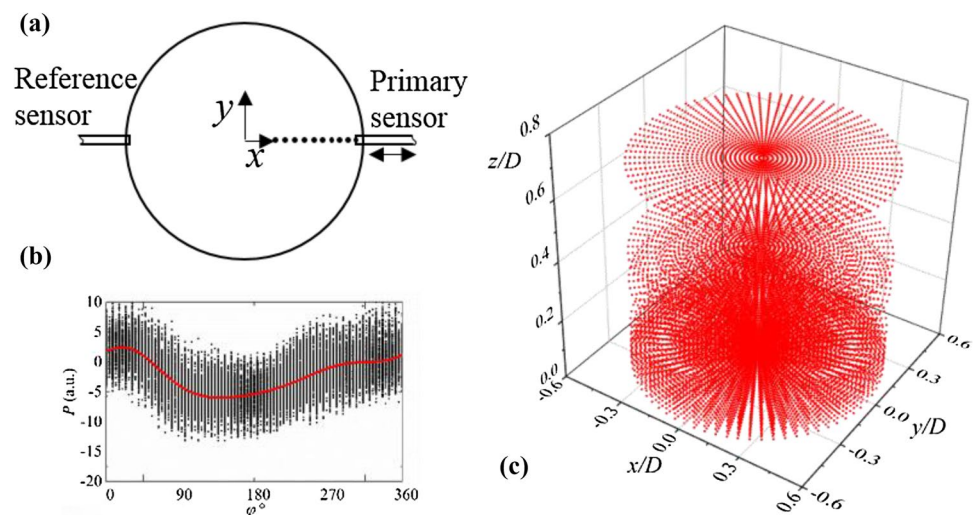


**Fig. 4** Illustration of the phase-averaging measurements using two acoustic sensors: diagram of the acoustic experiment (a), typical phase-averaging pressure pulsation (b), and a three-dimensional map of the measurement points (c)



vortex angular position does not affect the uncertainty in the estimates of the core size  $\epsilon$ , since it is determined along the radial direction (with a spatial resolution of approximately 1 mm). Furthermore, the signal received from the moving microphone sensor was divided into averaging windows, which were determined from the reference signal generated by the fixed probe and had a length equal to the duration of one vortex precession period (Fig. 4b). Thus, the measured signal was averaged over thousands of PVC periods. Considering the periodicity of the precession motion of the vortex and transforming from the time variable to the angular one, we plotted the pressure distribution vs. the azimuth angle and the distances along the  $x$ - and  $z$ -axes. Thus, the signals were processed for different points, and the spatial pressure distribution was obtained, which is shown as a three-dimensional map in Fig. 4c.

As shown in Fig. 4a, the acoustic sensor tip that acquires the instantaneous pressure traverses the flow along the radial direction. Therefore, the pressure tap of the probe is oriented tangentially to the major (tangential and axial) components of the swirling flow. The radial velocity, which in the case of the positive direction, i.e., from the center, contributes to the dynamic component of the acquired pressure, has a significantly lower value in a high-swirl flow than the axial and tangential velocities, which are mainly related to the static pressure level (Gupta et al. 1984). Thus, phase-averaged pressure distributions were used to estimate the vortex parameters and compare them with the parameters obtained from velocity distributions.

## 2.6 Identification of the structural parameters

Vorticity is a local quantity in the flow field  $\omega_z = (\partial v_y / \partial x) - (\partial v_x / \partial y)$ , while the circulation  $\Gamma$  quantifies the global measure of the vortex strength. It should be noted here that the entire vorticity in the flow field cannot be attributed solely to distinct vortices, since regions of pure shear also exhibit a certain amount of vorticity. The vortex core can be identified by different techniques, including methods based on the computation of velocity gradients. The common methods are the  $Q$  criterion and the  $\lambda_2$  criterion for the identification of vortical structures in turbulent flows (Jeong and Hussain 1995). Due to measurement uncertainty, the small-scale velocity fluctuations, and small spacing between the data points for PIV, velocity gradients can be erroneously perceived as coherent vertical structures determined by these vortex identification methods. In this study, we apply the approach from the paper (Graftieaux et al. 2001), where the authors use two scalar functions:  $\Gamma_1$  is used to identify the vortex center and  $\Gamma_2$  is used to estimate the vortex size. In this case, to construct such functions, the two-component instantaneous velocity distributions obtained by PIV are used. This method does not require a derivative

approximation in contrast to the  $\lambda_2$  criterion, and it works well when considering nonstationary flows (Bücker et al. 2012; Favrel et al. 2015; Huang and Green 2015; Widmann and Tropea 2017). According to (Graftieaux et al. 2001),  $\Gamma_1$  is introduced as follows:

$$\Gamma_1(P) = \frac{1}{N} \sum_S \frac{\text{PM} \times U_M}{\|\text{PM}\| \cdot \|U_M\|}, \quad (3)$$

where  $S$  is a rectangular elementary area with center at the point  $P$ ,  $M$  is a control point at which the velocity vector  $U_M$  is calculated, and  $N$  is the number of points within the area  $S$ . The vortex core size is calculated using the function  $\Gamma_2$ :

$$\Gamma_2(P) = \frac{1}{N} \sum_S \frac{\text{PM} \times (U_M - \tilde{U}_P)}{\|\text{PM}\| \cdot \|U_M - \tilde{U}_P\|}, \quad (4)$$

where  $\tilde{U}_P = (1/N) \sum_N U_M$  is the local convective velocity at the point  $P$ . The condition  $|\Gamma_1| > 0.95$  is used as a criterion to determine the vortex center; the condition  $2/\pi < |\Gamma_2| < 1$  is used to identify the area occupied by the vortex core. After calculating the function, we calculated the equivalent radius over the area to estimate the radius of the core. The parameter  $N$  plays the role of a spatial filter for the functions  $\Gamma_{1,2}$ , and  $N$  is used to remove small-scale turbulent fluctuations. Note that the size of the detected vortex core is weakly dependent on the parameter  $N$ , according to (Graftieaux et al. 2001). For our experimental conditions, the parameter is  $N = 120$ , which ensures that the functions  $\Gamma_1$  and  $\Gamma_2$  are averaged over a square with a side of  $11 \times 11$  points ( $S = 8 \times 8 \text{ mm}^2$ ). The vortex core circulation  $\Gamma$  can be calculated based on the streamwise vorticity component:  $\Gamma = \int_{\Sigma} \omega_z d\sigma$ , where the area  $\Sigma$  is the cross-sectional area of the vortex core obtained using the function  $\Gamma_2$ .

We also use the method of principal components or POD, which in a particular case is a mathematical procedure for expanding instantaneous velocity fields according to their contributions to the total energy of the flow (Holmes et al. 2012; Sirovich 1987); this approach has proved to be well suited for various turbulent flows (Gurka et al. 2006; Markovich et al. 2014; Oberleithner et al. 2011). In this case, POD is used as an alternative to the classic conditional-phase-averaging operator (Stöhr et al. 2011).

The POD method is based on finding an optimal basis of dimension  $N$  that can be used to approximate a set of instantaneous velocity fields:

$$u(\mathbf{x}, t) = \bar{u}(\mathbf{x}) + u'(\mathbf{x}, t) = \bar{u}(\mathbf{x}) + \sum_{i=1}^N a_i(t) \cdot \Phi_i(\mathbf{x}), \quad (5)$$

where  $a_i(t)$  is the projection of the instantaneous velocity field onto the  $i$ th POD mode. According to the method of



frame-by-frame POD (Sirovich 1987), the correlation matrix  $R_{ij} = \frac{1}{N} \langle u'(\mathbf{x}, t_i), u'(\mathbf{x}, t_j) \rangle$  is introduced, the eigenvalue problem is solved for this matrix, and the eigenvectors (time modes)  $a_i = [a_i(t_1), \dots, a_i(t_N)]$  are found that the eigenvalues  $\lambda_i$  have a clear physical meaning, namely, the amount of turbulence kinetic energy (TKE) transferred by this POD mode. Then, the POD function itself is a linear combination  $\Phi_i(\mathbf{x}) = \frac{1}{N\lambda_i} \sum_{k=1}^N a_i(t_k) \cdot u'(\mathbf{x}, t_k)$ . In this work, the POD modes are calculated using the algorithm suggested in (Sieber et al. 2016b).

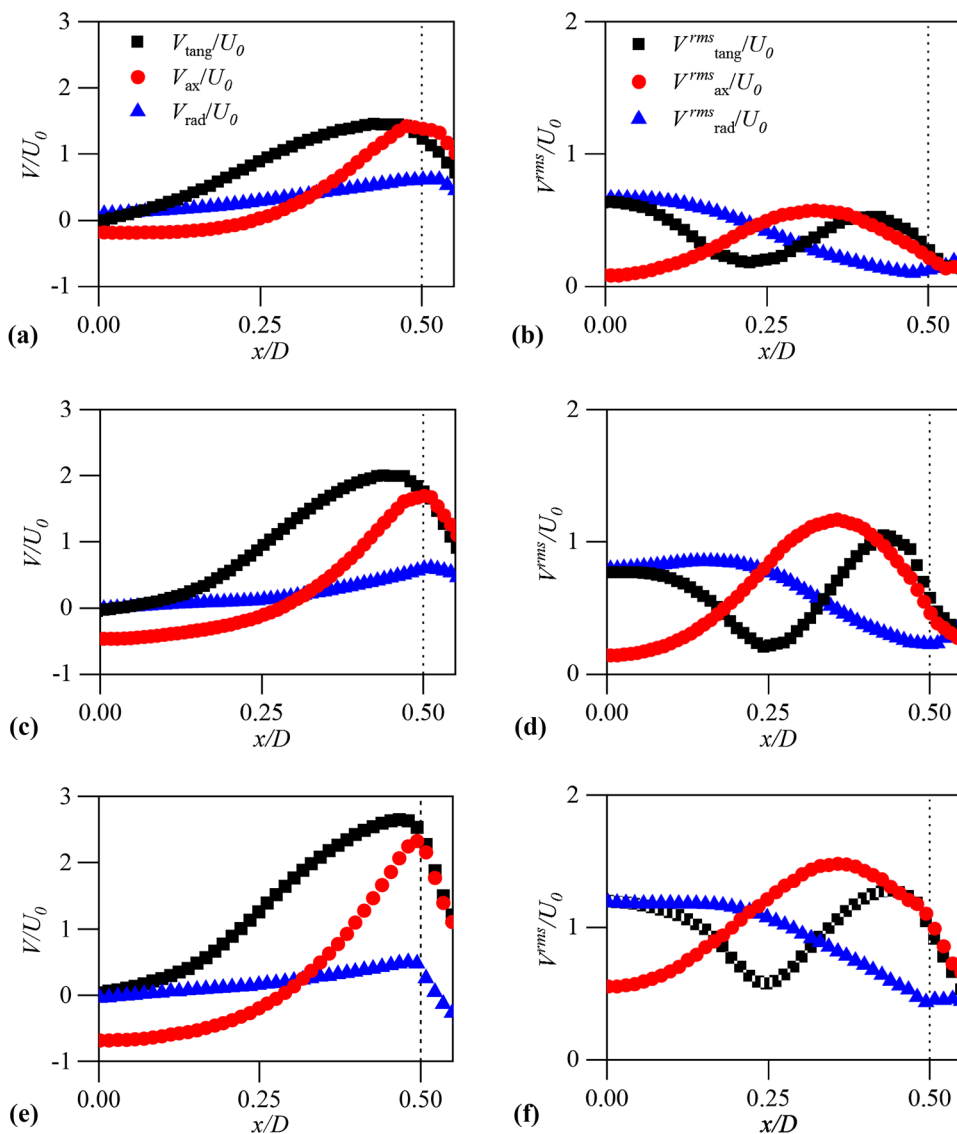
To determine the vortex core center from the measured phase-averaged pressure distributions, we used the minimum pressure criterion at the center of the vortex core. The size of the vortex core  $\varepsilon$  was defined as the width of half of the total pressure difference between the pressure in the center of the nozzle and the minimum pressure in the vortex core.

### 3 Results

#### 3.1 Characteristics of the flow

Figure 5a, c, e shows the time-averaged axial, tangential, and radial velocity profiles for three nozzle diameters ( $D=30, 40,$  and  $52$  mm) in the cross-section  $z=0.01D$ . The axial velocity profiles show the formation of a wide CRZ. At that time, some deviations from the generally assumed linear solid-body variation can also be noted in the tangential velocity distribution around the flow axis. The latter is attributed to the presence of a PVC (Cala et al. 2006). Figure 5b, d, f shows the root-mean-square (rms) distributions of the three velocity components, which are typical of high-swirl flows. The high values of the tangential rms velocity in this central region are attributed mainly to the inviscid pulsations

**Fig. 5** Time-averaged characteristics of the flow for  $z=0.01D$ : averaged velocity profiles  $S=1.4$  (a),  $S=1.8$  (c), and  $S=2.4$  (e), and the profiles of the rms of the velocity fluctuations for  $S=1.4$  (b),  $S=1.8$  (d), and  $S=2.4$  (f)



of the PVC and less to stochastic turbulence, as the shear in this region is low and the turbulence is also damped due to the flow rotation in the stable mode (Martinelli et al. 2012). The same inviscid pulsations of the PVC have an impact on the distribution of the axial rms velocity component.

The phase-averaged velocity distribution obtained by conditional averaging of approximately 90 PIV images for the current position of the vortex is presented in Fig. 6 for three different cases of  $S = 1.4$ , 1.8, and 2.4. The figure shows how the center of the vortex structure deviates from the central

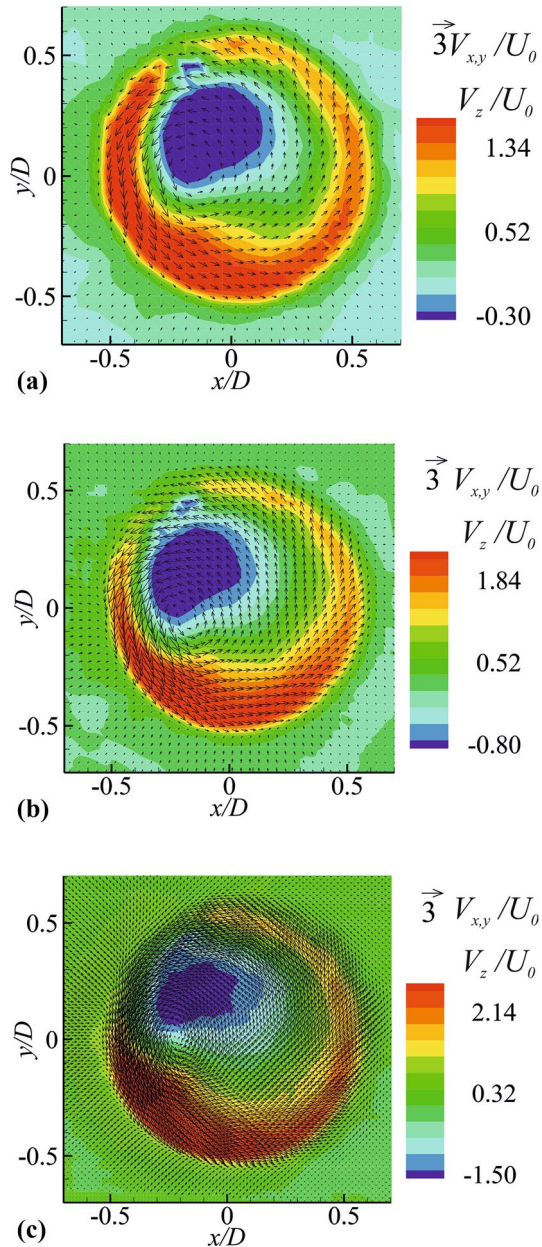


**Fig. 6** Phase-averaged velocity distributions for  $D=30$  mm and  $S=1.4$  (a),  $D=40$  mm and  $S=1.8$  (b), and  $D=52$  mm and  $S=2.4$  (c) in the cross-section  $z=0.01D$

position. At that time, the axial velocity maximum is located between the vortex core and the nozzle wall. The region of reverse flow is also shifted relative to the nozzle center. It should be noted that the map visualizes an “instantaneous” flow pattern that rotates together with the vortex core. It can be inferred that the phase-averaged distributions of the velocity for the three swirl numbers look very similar. Therefore, two cases ( $S = 1.4$ – $1.8$ ) are not displayed for brevity, and further analysis is only performed for the reference point  $S = 2.4$  and  $Re = 2.3 \times 10^4$ .

To gain insight into the averaged velocity field in the streamwise direction, we consider the vertical cross-section along the center of the swirler for the case of  $D=52$  mm. We use a planar two-component PIV system in the  $x$ - $z$  plane of the laser sheet (Fig. 2). Figure 7 illustrates the streamlines, which show that the strongly swirling flow is pressed to the nozzle walls, and a CRZ is formed in the center of the flow that penetrates deep into the nozzle. The formation of the CRZ is a good indicator of the PVC effect, which is widely covered in the literature (Syred 2006; Yazdabadi et al. 1994). The figure also shows the isocontours of the axial contribution of the dimensionless TKE  $\langle E_z \rangle / U_0^2$ . The maximum in the distribution occurs at a distance  $x \approx 0.3$ – $0.4D$  from the axis of the chamber nozzle, which corresponds to the maximum generation of turbulence in this zone.

## 3.2 Identification of the precessing vortex structure (reference point)

### 3.2.1 Statistical method for estimating the structural parameters of the PVC

To estimate the vortex parameters directly from all the PIV statistics, we used the instantaneous three-component velocity distributions in the  $x$ - $y$  measurement cross-section (see

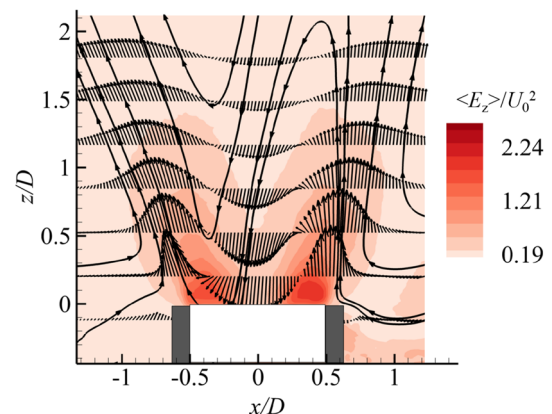


**Fig. 7** Streamlines and isocontours of the axial contribution in the TKE for the streamwise direction ( $x$ - $z$  cross-section,  $S=2.4$  and  $D=52$  mm)

Fig. 2) at a height of  $z=0.01D$ . The locus of the vortex center points determined with the help of the scalar function  $\Gamma_1$  (2) calculated for each of the 5000 instantaneous velocity distributions in the cross-section  $z/D=0.01$  is shown in Fig. 8a. Approximately 300 PIV images were excluded (6% of the total value), so that the vortex core was not identified within the nozzle area. As can be seen from the figure, the trajectory of the precessing core in this cross-section is close to a circle (the ellipticity is less than 4%). Figure 8b shows a normal quantile–quantile (Q–Q) plot of the dimensionless precession radius  $a/D = \sqrt{x^2 + y^2}/D$  plotted by the locus of the vortex centers. If we accept the hypothesis of a normal distribution, we can estimate the average value of the PVC radius  $a/D$  as 0.26 with a standard deviation of 0.027. This result indicates that the flow is quasi-periodic in space.

The equivalent vortex radius  $\varepsilon$  is calculated as  $\varepsilon = \sqrt{\Sigma/\pi}$ , where  $\Sigma$  is the area occupied by the vortex core (criteria  $2/\pi < |\Gamma_2| < 1$ ). Q–Q plots of the dimensionless vortex core radius  $\varepsilon/D$  calculated using the function  $\Gamma_2$  (3) are presented in Fig. 9a. Again, assuming a normal distribution, we can estimate the average value of the precessing radius  $\varepsilon/D$  as 0.16 with a standard deviation  $\sigma=0.037$ . The vortex

circulation  $\Gamma/DU_0$  is calculated using the integral definition  $\Gamma = \int_{\Sigma} \omega_z d\sigma$ . Based on the hypothesis of a normal distribution, the average value of the vortex circulation  $\Gamma/DU_0$  can be estimated as 5.5 with a standard deviation  $\sigma=1.51$ .

It should be noted that the above statistics are obtained for more than 750 thousand precession periods, which also indicates that the precession of the vortex core under these conditions is a highly quasi-periodic process in time and space.

### 3.2.2 POD versus phase-averaging analysis

The spectrum of POD modes plotted based on 5000 PIV images in the cross-section  $z=0.01D$  is shown in Fig. 10. In the spectrum, two of the most energetic modes include more than 34% of the total TKE, while the third mode carries only 3% of the TKE. If we plot the dependence of the time modes in the form of Lissajous curves  $a_1(a_2)$  (see Fig. 10b), we can see that the modes lag behind each other by  $\pi/2$  (Markovich et al. 2016; Oberleithner et al. 2011). This indicates that the first two modes are associated with a nonstationary phenomenon that arises in the flow in the form of a PVC.

**Fig. 8** Determination of the radius of the vortex precession: the locus of the vortex center from the instantaneous velocity distributions (a), and a Q–Q plot of the dimensionless vortex core radius  $a/D$  (the upper and lower percentile lines are limited to a 95% confidence band) (b)

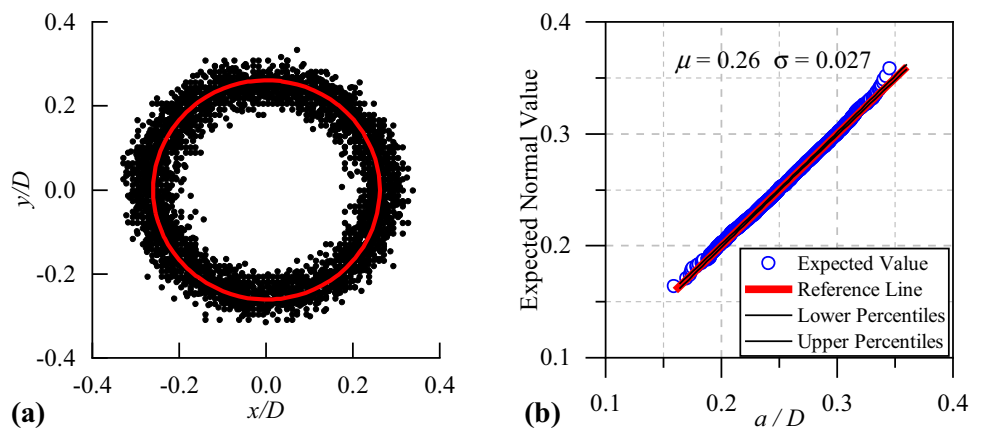


**Fig. 9** Distributions of the vortex core radius and circulation: a Q–Q plot of the dimensionless vortex core radius  $\varepsilon/D$  (a), and a Q–Q plot of the dimensionless circulation  $\Gamma/(DU_0)$  (the upper and lower percentiles' line is limited to a 95% confidence band) (b)

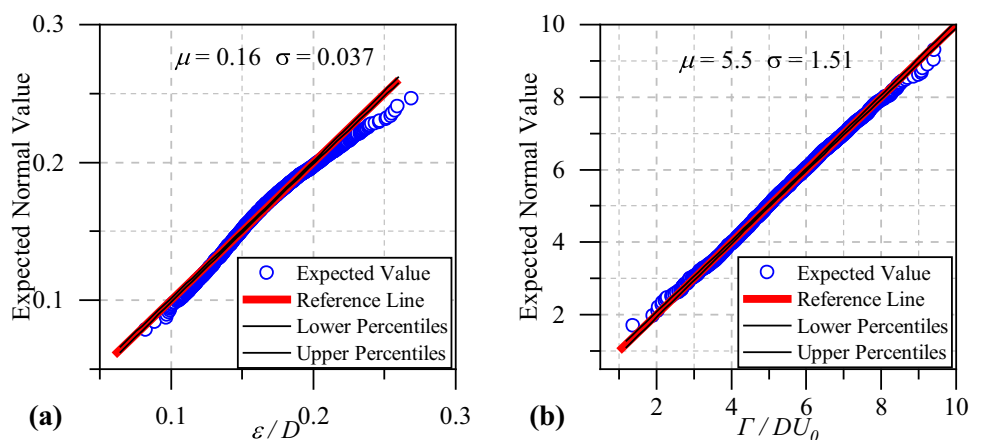


**Fig. 10** Spectral analysis of the POD modes obtained from the three-component velocity distribution in the cross-section  $z=0.01D$

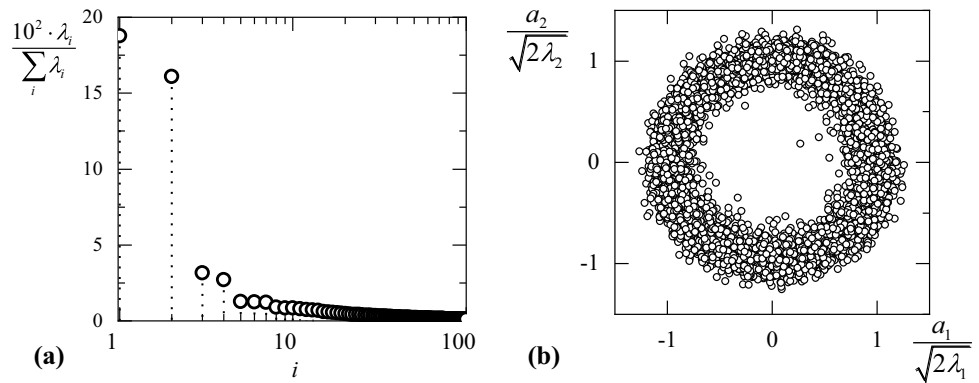
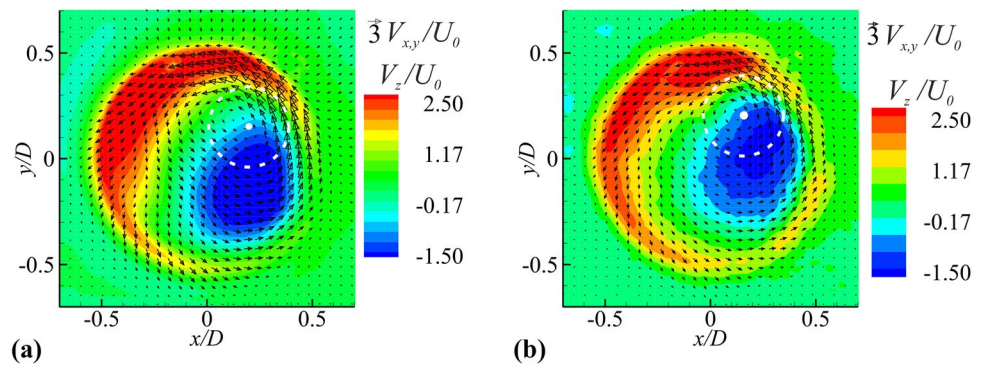


**Fig. 11** “Instantaneous” velocity distribution: obtained by POD analysis using Eq. (6) (a) and obtained by phase averaging (b). The white spot and the dashed circle show the center and boundary of the PVC, respectively, determined using the functions  $\Gamma_1$  and  $\Gamma_2$  in the cross-section  $z=0.01D$



We now construct the velocity distribution of the reduced dimension to obtain the structural parameters of the PVC. Figure 11a shows the distribution of the three velocity components, which is a superposition of the mean flow and two POD modes [e.g., in (Markovich et al. 2014)]:

$$U_{\text{POD}}(\mathbf{x}) \approx U(\mathbf{x}) + R_1 \varphi_1(\mathbf{x}) \cos \theta_0 + R_2 \varphi_2(\mathbf{x}) \sin \theta_0, \quad (6)$$

where  $U(\mathbf{x})$  is the mean field of the flow,  $\varphi_{1,2}$  are the two most energetic POD modes,  $R_i = \sqrt{2\lambda_i}$  are the coefficients of the first two POD modes, and  $\theta_0=45^\circ$  is the azimuthal angle. The vortex core shown in the velocity distribution was found with the help of the functions  $\Gamma_1$  and  $\Gamma_2$ . For a comparison, Fig. 11b also shows the phase-averaged velocity distribution for  $\theta_0 \approx 45^\circ$ . There is a good correlation between these two distributions obtained by two independent approaches (POD and phase-averaging).

Phase-averaging was also carried out for various angular positions of the precessing vortex. The distributions for several phase angles are constructed in Fig. 12 with a step  $\theta \approx 45^\circ$ . Phase-averaging was performed with a resolution of  $\Delta\theta = \pm 8^\circ$  with the corresponding statistics of approximately 90 images in each distribution. It is shown that the shape and size of the vortex, and the precession radius vary slightly during one revolution. POD analysis, in contrast to phase averaging, does not provide information on the temporal

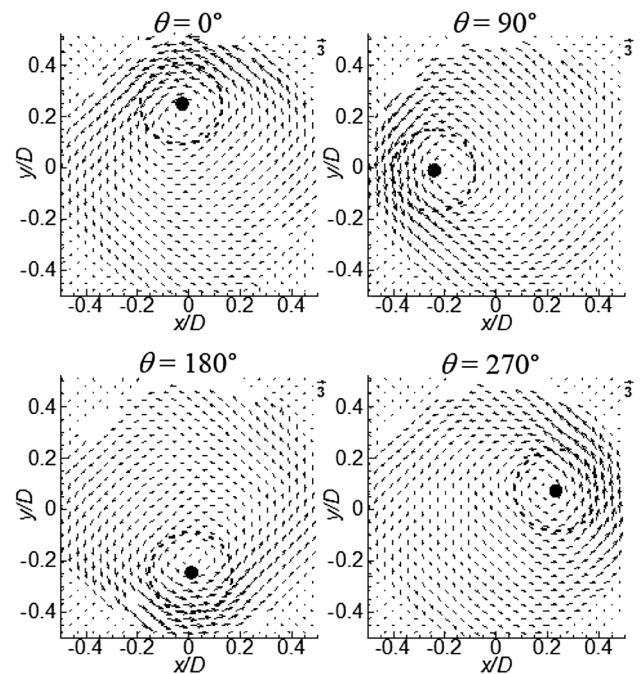


**Fig. 12** Phase-averaged distributions of the two velocity components in the cross-section  $z=0.01D$



**Fig. 13** Distribution of the dimensionless vorticity in the cross-section  $z/D=0.01$  and estimates of the vortex location and size using the functions  $\Gamma_1$  and  $\Gamma_2$ : instantaneous (a) and phase-averaged (90 snapshots) (b)

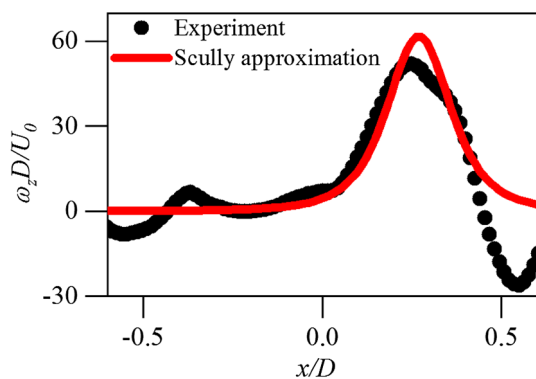
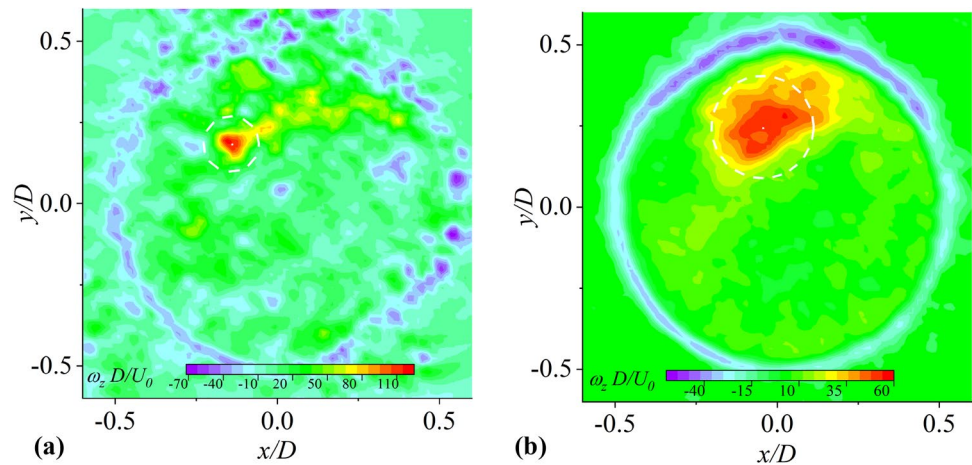


**Fig. 14** Testing of the obtained structural parameters of the helical vortex from all the statistics using the model Scully vortex distribution of the axial vorticity

evolution of the vortex core motion during one revolution; moreover, it is also impossible to obtain the structural parameters of the vortex for different  $x$ - $y$  cross-sections along the height  $z$ .

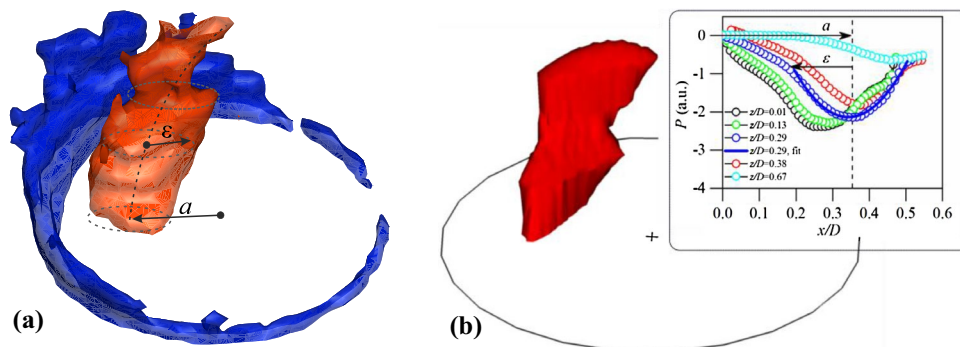


**Fig. 15** PVC visualization using the isosurfaces of the phase-averaged distributions of the axial vorticity (the red color shows positive vorticity, and the blue color indicates a negative vorticity, associated with the outer mixing layer beyond the nozzle boundaries) (a) and

The distribution of the instantaneous vorticity field demonstrates that the vortex structure identified using the functions  $\Gamma_1$  and  $\Gamma_2$  correlates with the vorticity maximum presented in Fig. 13a. Nevertheless, it is difficult to unambiguously determine the vortex dimensions from the axial vorticity distribution, so we have to use phase averaging (with the statistics of approximately 90 images) and the scalar functions  $\Gamma_1$  and  $\Gamma_2$  (Fig. 13b) to estimate the structural parameters  $a$ ,  $\epsilon$ , and  $\Gamma$ .

In addition, the obtained PVC parameters can be tested by analyzing the axial vorticity distribution along the line that passes through the vortex center (Fig. 14b). To estimate these parameters, we use the Scully vortex model (Scully 1975):  $\omega_{z, \text{Scully}} = (\Gamma \cdot \epsilon^2 / \pi) (1 / ((x - a)^2 + \epsilon^2)^2)$ , which is suitable for describing a turbulent vortex flow with a concentrated vorticity. The parameters  $a$ ,  $\epsilon$ , and  $\Gamma$  found using the functions  $\Gamma_1$  and  $\Gamma_2$  from all the statistics (4700 snapshots) were applied to the Scully vortex vorticity distribution.

using the isosurfaces of the phase-averaged pressure distributions (the inset shows the radial direction through the PVC center with definition of the parameters  $a$  and  $\epsilon$ ) (b)

### 3.2.3 Testing of the local helical symmetry

To directly determine the helical vortex pitch, we performed phase-averaged velocity measurements for several cross-sections in the range  $z=0.01D-0.5D$ . The three-dimensional distribution of the isosurfaces of the axial vorticity component  $\omega_z$  is shown

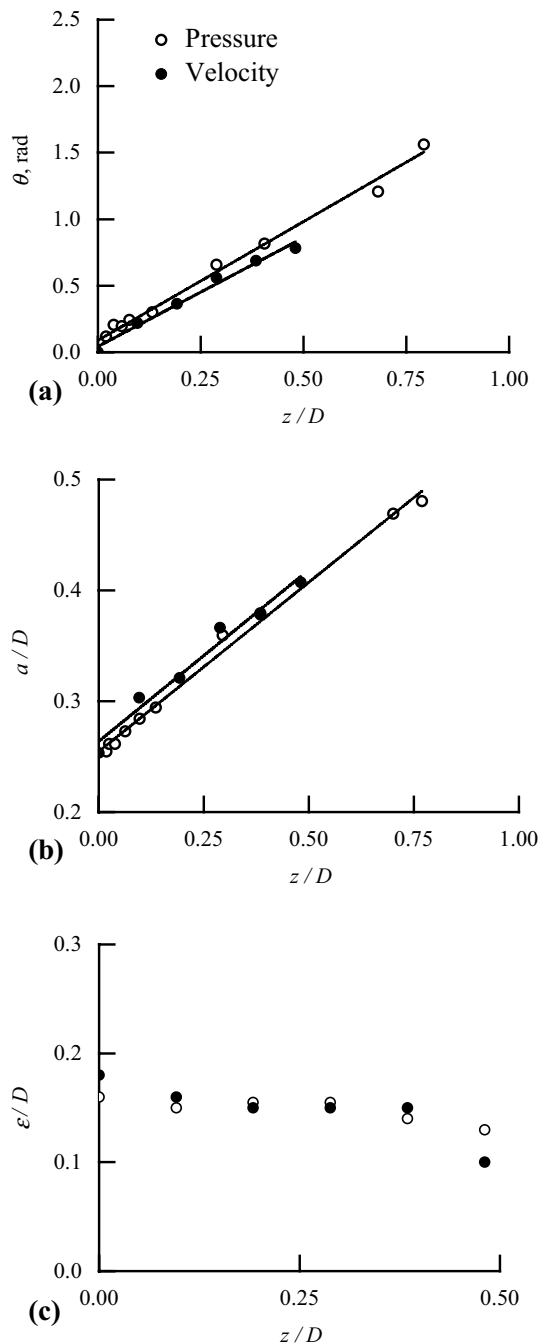


**Fig. 16** Evolution of the PVC parameters: the turn angle vs. the height above the nozzle (a), the precession radius vs. the height above the nozzle (b), and the vortex core radius vs. the height above the nozzle (c)

in Fig. 15a. At a height greater than  $z>0.6D$ , it is impossible to identify the vortex core, because almost immediately after the nozzle, the vortex core dissipates, and only a short, slightly curved section of the vortex is observed in the experiment. Most likely, a similar vortex structure was obtained in (Akhmetov et al. 2004), where a vortex in the form of a “bandy” was identified. It is interesting that the size of the vortex core  $\epsilon$  is a nearly constant function of the height  $z$ . This implies that at  $z<0.6D$ , the vortex is stable and has a fixed size, but above this height, the vortex dissipates very rapidly. However, in these cross-sections, we can distinguish the local helical geometry. The PVC has the shape of a long spiral (the parameter  $a$  is much smaller than  $h$ ); here, a left-handed vortex structure is observed, because it rotates against the swirl direction (counterclockwise rotation).

Pressure isosurfaces with negative pressure pulsations plotted using the phase-averaging technique are shown in Fig. 15b. The geometry of the vortex core is very similar to the results obtained from the phase-averaged distribution of the axial vorticity component. Again, the size of the vortex core  $\epsilon$  does not show significant changes as a function of the height  $z$ , and the decay of the pressure amplitude is rapid (the vortex core is not identified for  $z>0.8D$ ).

The measurements of two independent experiments with the phase-averaged velocity and pressure distributions showed a linear increase in the azimuth rotation angle of the vortex core  $\theta$  (Fig. 16a). The vortex core location at various heights above the nozzle was determined from the measured velocity distributions using algorithm (2). The vortex core location in the pressure distribution was determined from the minimum pressure corresponding to the center of the vortex structure. Then, the pitch of the helical structure could be locally determined based on the measurement of the angular position of the vortex center along the axial coordinate by formula  $h = 2\pi dz / \partial\theta$ . As shown in Fig. 16b, immediately after the chamber nozzle, the vortex decays, and the value of the precession radius  $a/D$  also increases linearly with the distance from the vortex chamber nozzle until the full

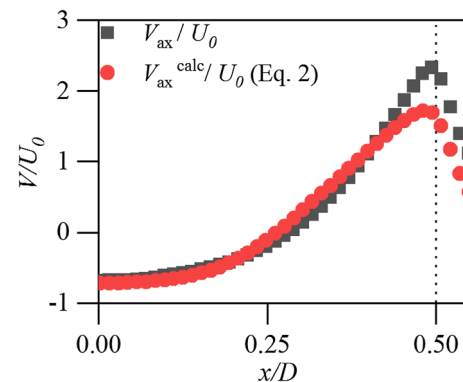


**Fig. 17** Testing of the helical symmetry of the mean axial and tangential velocity profiles in the cross-section  $z=0.01D$

**Table 1** Comparison of the vortex parameters for the helical vortex model estimated by various techniques

Estimate method for the structural parameters ( $z=0.01D$ )	$\Gamma/DU_0$	$a/D$	$\varepsilon/D$	$h/D$
From instantaneous distributions (4700 PIV images)	5.5	0.26	0.16	–
From distributions of reduced dimension (average flow + the first two POD modes)	5.85	0.26	0.18	–
From phase-averaged PIV distributions of velocities (averaging over 90 images)	5.9	0.26	0.18	3.38
From phase-averaged pressure distributions by acoustic sensors	–	0.26	0.16	3.3

disappearance at  $z/D \approx 0.8$ . Nearly, the same radius of the vortex core as a function of height is shown in Fig. 16c.

We now implicitly test the helical symmetry condition of Eq. (2) and apply the obtained helical pitch  $h$  to the mean axial and tangential velocity profiles (Fig. 5a). This confirms that the helical symmetry is preserved in the region  $x < 0.4D$ , excluding thin layers adjacent to the wall (Fig. 17). The parameter  $u_{ax}$  equals  $-0.68U_0$ . The parameter  $h$  is given in Table 1.

### 3.3 Overview of the PVC parameters

All estimates of the vortex parameters are given in Table 1. The first three lines of the parameters are determined using the functions  $\Gamma_1$  and  $\Gamma_2$ . The estimates of the parameters  $\Gamma$ ,  $a$ , and  $\varepsilon$  determined directly from all the statistics of the PIV images and for the reduced-dimension model (with two POD modes considered) are in agreement with each other. The most complete method for determining all the vortex parameters is the conditional (phase) averaging of the velocity distributions at various heights above the nozzle, which allows us to distinguish the pitch of the helical flow symmetry. The parameters obtained from the pressure distribution are consistent.

The helical vortex model was used to calculate the PVC frequency (see “Appendix”). The Strouhal number calculated by the formula  $Sh_{th} = f_{th} \cdot D/U_0$  gives a value of 1.25 for the range of parameters calculated from the PVC parameters given in Table 1 for the experimentally determined value  $Sh_{exp} = 1.56$ . To explain this discrepancy (20%), it should be considered that the analytical model depends on a number of assumptions, which may not fully comply with the actual situation. Nevertheless, the estimate of the PVC frequency obtained in this study confirms that the helical vortex model provides a fast and precise prediction of the dominant flow dynamics.

## 4 Conclusions

A nonstationary flow with the formation of a PVC at the exit of a tangential swirler was experimentally analyzed using an SPIV system and acoustic sensors. It was shown by POD analysis that the PVC makes a significant contribution (more than 34%) to the TKE, which makes this flow a convenient object for testing the model of a helical precessing vortex.

Using two scalar functions  $\Gamma_1$  and  $\Gamma_2$ , estimates of the model vortex parameters (core radius, vortex precession radius, and vortex intensity) were obtained using statistical data of the vortex locations from uncorrelated PIV images when the precession motion phase was random at the time of the velocity measurement. Alternatively, vortex core parameters were determined from the reconstructed velocity distribution which includes the two most energetic POD modes. In addition, these parameters were compared with those obtained from the phase-averaged velocity distributions recovered relative to a particular phase of the vortex core. The phase-averaged data showed that the size of the core and the radius of precession vary insignificantly. The statistical analysis of the vortex parameters obtained with the help of the scalar functions  $\Gamma_1$  and  $\Gamma_2$  showed that the radius of precession changes by 10%, the core radius changes by 25%, and the vortex circulation changes by no more than 30%. All of these approaches used to determine the vortex parameters were found to be equivalent. However, using the statistical analysis of uncorrelated PIV images, it was not possible to evaluate the pitch of the helical structure, in contrast to the conditional averaging technique.

All of the approaches were shown to provide access to the structural parameters of the PVC. The precession frequency could be estimated with an uncertainty of 20%. This is a reasonable accuracy, especially considering the strong assumptions made for the PVC frequency estimation (an inviscid fluid and an infinite helical structure in a cylindrical tube). It should be noted that previous attempts to test the theory were based on indirect parameters calculated from time-averaged velocity distributions. This work is a first step in the use of the helical vortex model, which can be an effective tool for predicting the features of a swirl flow with a PVC.

**Acknowledgments** The research was supported by the Russian Science Foundation (Project No. 18-79-00229).

## Appendix: Calculation of PVC frequency

Considering all contributions to the PVC frequency (Table 2) and following (Alekseenko et al. 1999, 2007), we obtain the following formula for calculating the PVC frequency based on the model of a helical vortex in a tube:  $f_{ih}(\Gamma, \varepsilon, a, l, u_{ax}, R) = f_c + f_\tau + f_R + f_\beta$ .

**Table 2** Contributions of different effects to the PVC frequency

Contribution	Formula
Curvature	$f_c = -\frac{1}{8\pi^2} \frac{\Gamma}{a^2} \frac{1}{\tau\sqrt{1+\tau^2}} \ln \left[ \frac{a}{\epsilon} (1 + \tau^2) \right]$
Torsion	$f_\tau = -\frac{1}{8\pi^2} \frac{\Gamma}{a^2} \frac{1}{\tau\sqrt{1+\tau^2}} \left[ \ln \left( \frac{\tau}{1+\tau^2} \right) + \frac{1+1.455\tau+1.723\tau^2+0.711\tau^3+0.616\tau^4}{\tau+0.486\tau^2+1.176\tau^3+\tau^4} - 2 \frac{\sqrt{1+\tau^2}}{\tau} - \frac{1}{4} \right]$
Nozzle walls	$f_R = \frac{1}{4\pi^2} \frac{\Gamma}{a^2} \frac{1+\tau^2}{\tau^2} \left( \frac{a^2}{R^2-a^2} - k \cdot \ln \frac{R^2-a^2}{R^2} \right)$
Velocity on the axis	$f_\beta = -\frac{1}{4\pi^2} \frac{\Gamma}{a^2} \frac{\beta}{\tau^2}$

where  $k = \frac{1}{12} \left[ \frac{9\eta}{(1+\eta^2)^{1/2}} - \frac{7\eta^3}{(1+\eta^2)^{3/2}} - \frac{3\tau}{(1+\tau^2)^{1/2}} + \frac{\tau^3}{(1+\tau^2)^{3/2}} \right]$ ,  $l = h/2\pi$ ,  
 $\beta = u_{ax} 2\pi l / \Gamma$ ,  $\tau = l/a$ ,  $\eta = l/R$ ,  $\tilde{x} = 2x \exp \left[ \sqrt{1 + (x^2/l^2)} - 1 \right] / \left( \sqrt{1 + (x^2/l^2)} + 1 \right)$ ,  $\tilde{x} = \tilde{a}$ ,  $\tilde{R}$

## References

- Ahmed MMA, Birouk M (2018) Effect of fuel nozzle geometry and airflow swirl on the coherent structures of partially premixed methane flame under flashback conditions. *Exp Thermal Fluid Sci* 99:304–314. <https://doi.org/10.1016/j.expthermflusc.2018.08.003>
- Akhmetov D, Nikulin V, Petrov V (2004) Experimental study of self-oscillations developing in a swirling-jet flow. *Fluid Dyn* 39:406–413
- Alekseenko SV, Kuibin PA, Okulov VL, Shtork SI (1999) Helical vortices in swirl flow. *J Fluid Mech* 382:195–243. <https://doi.org/10.1017/S0022112098003772>
- Alekseenko SV, Kuibin PA, Okulov VL (2007) Theory of concentrated vortices: an introduction. Springer, New York
- Alekseenko SV, Abdurakipov SS, Hrebtov MY, Tokarev MP, Dulin VM, Markovich DM (2018) Coherent structures in the near-field of swirling turbulent jets: a tomographic PIV study. *Int J Heat Fluid Flow* 70:363–379. <https://doi.org/10.1016/j.ijheatfluidflow.2017.12.009>
- Anacleto PM, Fernandes EC, Heitor MV, Shtork SI (2003) Swirl flow structure and flame characteristics in a model lean premixed combustor. *Combust Sci Technol* 175:1369–1388
- Benjamin TB (1962) Theory of the vortex breakdown phenomenon. *J Fluid Mech* 14:593. <https://doi.org/10.1017/S0022112062001482>
- Bücker I, Karhoff D-C, Klaas M, Schröder W (2012) Stereoscopic multi-planar PIV measurements of in-cylinder tumbling flow. *Exp Fluids* 53:1993–2009. <https://doi.org/10.1007/s00348-012-1402-5>
- Cala CE, Fernandes EC, Heitor MV, Shtork SI (2006) Coherent structures in unsteady swirling jet flow. *Exp Fluids* 40:267–276. <https://doi.org/10.1007/s00348-005-0066-9>
- Candel S, Durox D, Schuller T, Bourgooin J-F, Moeck JP (2014) Dynamics of swirling flames. *Annu Rev Fluid Mech* 46:147–173
- Cassidy JJ, Falvey HT (1969) Observations of unsteady flow arising after vortex breakdown. *J Fluid Mech* 41:727–736
- Chanaud RC (1965) Observations of oscillatory motion in certain swirling flows. *J Fluid Mech* 21:111–127. <https://doi.org/10.1017/S0022112065000083>
- Chinnici A, Arjomandi M, Tian ZF, Lu Z, Nathan GJ (2015) A novel solar expanding-vortex particle reactor: influence of vortex structure on particle residence times and trajectories. *Sol Energy* 122:58–75. <https://doi.org/10.1016/j.solener.2015.08.017>
- Cozzi F, Coghe A, Sharma R (2018) Analysis of local entrainment rate in the initial region of isothermal free swirling jets by Stereo PIV. *Exp Thermal Fluid Sci* 94:281–294. <https://doi.org/10.1016/j.expthermflusc.2018.01.013>
- Derksen JJ, Van den Akker HEA (2000) Simulation of vortex core precession in a reverse-flow cyclone. *AIChE J* 46:1317–1331. <https://doi.org/10.1002/aic.690460706>
- Dörfler P, Sick M, Coutu A (2012) Flow-Induced Pulsation and Vibration in Hydroelectric Machinery: Engineer's Guidebook for Planning, Design and Troubleshooting. Springer, New York
- Faler JH, Leibovich S (1978) An experimental map of the internal structure of a vortex breakdown. *J Fluid Mech* 86:313. <https://doi.org/10.1017/S0022112078001159>
- Favrel A, Müller A, Landry C, Yamamoto K, Avellan F (2015) Study of the vortex-induced pressure excitation source in a Francis turbine draft tube by particle image velocimetry. *Exp Fluids*. <https://doi.org/10.1007/s00348-015-2085-5>
- Garg AK, Leibovich S (1979) Spectral characteristics of vortex breakdown flowfields. *Phys Fluids* 1958–1988(22):2053–2064
- Gomez-Ramirez D, Ekkad SV, Moon H-K, Kim Y, Srinivasan R (2017) Isothermal coherent structures and turbulent flow produced by a gas turbine combustor lean pre-mixed swirl fuel nozzle. *Exp Thermal Fluid Sci* 81:187–201
- Gorbunova A, Klimov A, Molevich N, Moralev I, Porfiriev D, Sugak S, Zavershinskii I (2016) Precessing vortex core in a swirling wake with heat release. *Int J Heat Fluid Flow* 59:100–108. <https://doi.org/10.1016/j.ijheatfluidflow.2016.03.002>
- Graftieaux L, Michard M, Grosjean N (2001) Combining PIV, POD and vortex identification algorithms for the study of unsteady turbulent swirling flows. *Meas Sci Technol* 12:1422–1429
- Grimble TA, Agarwal A (2015) Characterisation of acoustically linked oscillations in cyclone separators. *J Fluid Mech* 780:45–59
- Grosjean N, Graftieaux L, Michard M, Hübner W, Tropea C, Volkert J (1997) Combining LDA and PIV for turbulence measurements in unsteady swirling flows. *Meas Sci Technol* 8:1523–1532
- Guo X, Zhang B (2018) Computational investigation of precessing vortex breakdown and energy separation in a Ranque-Hilsch vortex tube. *Int J Refrig* 85:42–57. <https://doi.org/10.1016/j.ijrefrig.2017.09.010>
- Gupta K, Lilley DG, Syred N (1984) Swirl flows. Abacus Press, Kent
- Gurka R, Liberzon A, Hetsroni G (2006) POD of vorticity fields: a method for spatial characterization of coherent structures. *Int J Heat Fluid Flow* 27:416–423. <https://doi.org/10.1016/j.ijheatfluidflow.2006.01.001>
- Holmes P, Lumley JL, Berkooz G, Rowley CW (2012) Turbulence, coherent structures, dynamical systems and symmetry. Cambridge University Press, Cambridge
- Huang Y, Green MA (2015) Detection and tracking of vortex phenomena using Lagrangian coherent structures. *Exp Fluids* 56:147. <https://doi.org/10.1007/s00348-015-2001-z>
- Jeong J, Hussain F (1995) On the identification of a vortex. *J Fluid Mech* 285:69. <https://doi.org/10.1017/S0022112095000462>
- Klimov A, Bityurin V, Tolkunov B, Zhirnov K, Plotnikova M, Minko K, Kutlaliyev V (2008) Longitudinal vortex plasmoid created by capacity HF discharge. In: 46th AIAA Aerospace Sciences Meeting and Exhibit. Presented at the 46th AIAA Aerospace Sciences Meeting and Exhibit, American Institute of Aeronautics and Astronautics, Reno, Nevada. <https://doi.org/10.2514/6.2008-1386>
- Kuibin PA, Okulov VL (1998) Self-induced motion and asymptotic expansion of the velocity field in the vicinity of a helical vortex filament. *Phys Fluids* 10:607–614. <https://doi.org/10.1063/1.869587>
- Kulkarni AA, Ranade VV, Rajeev R, Koganti SB (2009) Pressure drop across vortex diodes: experiments and design guidelines. *Chem Eng Sci* 64:1285–1292. <https://doi.org/10.1016/j.ces.2008.10.060>



- Kurosaka M (1982) Acoustic streaming in swirling flow and the Ranque—Hilsch (vortex-tube) effect. *J Fluid Mech* 124:139. <https://doi.org/10.1017/S0022112082002444>
- Liang H, Maxworthy T (2005) An experimental investigation of swirling jets. *J Fluid Mech* 525:115–159. <https://doi.org/10.1017/S0022112004002629>
- Litvinov IV, Shtork SI, Kuibin PA, Alekseenko SV, Hanjalić K (2013) Experimental study and analytical reconstruction of precessing vortex in a tangential swirl. *Int J Heat Fluid Flow* 42:251–264. <https://doi.org/10.1016/j.ijheatfluidflow.2013.02.009>
- Litvinov IV, Sharaborin DK, Shtork SI (2015) Finding of parameters of helical symmetry for unsteady vortex flow based on phase-averaged PIV measurement data. *Thermophys Aeromech* 22:647–650. <https://doi.org/10.1134/S0869864315050133>
- Litvinov I, Shtork S, Gorelikov E, Mitryakov A, Hanjalić K (2018) Unsteady regimes and pressure pulsations in draft tube of a model hydro turbine in a range of off-design conditions. *Exp Therm Fluid Sci* 91:410–422
- Lucca-Negro O, O’Doherty T (2001) Vortex breakdown: a review. *Prog Energy Combust Sci* 27:431–481. [https://doi.org/10.1016/S0360-1285\(00\)00022-8](https://doi.org/10.1016/S0360-1285(00)00022-8)
- Mak H, Balabani S (2007) Near field characteristics of swirling flow past a sudden expansion. *Chem Eng Sci* 62:6726–6746
- Markovich DM, Abdurakipov SS, Chikishev LM, Dulin VM, Hanjalić K (2014) Comparative analysis of low- and high-swirl confined flames and jets by proper orthogonal and dynamic mode decompositions. *Phys Fluids* 26:065109. <https://doi.org/10.1063/1.4884915>
- Markovich DM, Dulin VM, Abdurakipov SS, Kozinkin LA, Tokarev MP, Hanjalić K (2016) Helical modes in low- and high-swirl jets measured by tomographic PIV. *J Turbul* 17:678–698. <https://doi.org/10.1080/14685248.2016.1173697>
- Martinelli F, Olivani A, Coghe A (2007) Experimental analysis of the precessing vortex core in a free swirling jet. *Exp Fluids* 42:827–839. <https://doi.org/10.1007/s00348-006-0230-x>
- Martinelli F, Cozzi F, Coghe A (2012) Phase-locked analysis of velocity fluctuations in a turbulent free swirling jet after vortex breakdown. *Exp Fluids* 53:437–449. <https://doi.org/10.1007/s00348-012-1296-2>
- Moeck JP, Bourgooin J, Durox D, Schuller T, Candel S (2012) Nonlinear interaction between a precessing vortex core and acoustic oscillations in a turbulent swirling flame. *Combust Flame* 159:2650–2668. <https://doi.org/10.1016/j.combustflame.2012.04.002>
- Oberleithner K, Sieber M, Nayeri CN, Paschereit CO, Petz C, Hege H-C, Noack BR, Wygnanski I (2011) Three-dimensional coherent structures in a swirling jet undergoing vortex breakdown: stability analysis and empirical mode construction. *J Fluid Mech* 679:383–414. <https://doi.org/10.1017/jfm.2011.141>
- Oberleithner K, Paschereit CO, Seele R, Wygnanski I (2012) Formation of turbulent vortex breakdown: intermittency, criticality, and global instability. *AIAA J* 50:1437–1452. <https://doi.org/10.2514/1.J050642>
- Oberleithner K, Paschereit CO, Wygnanski I (2014) On the impact of swirl on the growth of coherent structures. *J Fluid Mech* 741:156–199. <https://doi.org/10.1017/jfm.2013.669>
- Pandare A, Ranade VV (2015) Flow in vortex diodes. *Chem Eng Res Des* 102:274–285. <https://doi.org/10.1016/j.cherd.2015.05.028>
- Percin M, Vanierschot M, van Oudheusden BW (2017) Analysis of the pressure fields in a swirling annular jet flow. *Exp Fluids* 58:166. <https://doi.org/10.1007/s00348-017-2446-3>
- Piralishvili ShA, Polyayev VM (1996) Flow and thermodynamic characteristics of energy separation in a double-circuit vortex tube—an experimental investigation. *Exp Thermal Fluid Sci* 12:399–410. [https://doi.org/10.1016/0894-1777\(95\)00122-0](https://doi.org/10.1016/0894-1777(95)00122-0)
- Prasad AK, Jensen K (1995) Scheimpflug stereocamera for particle image velocimetry in liquid flows. *Appl Opt* 34:7092–7099. <https://doi.org/10.1364/AO.34.007092>
- Scarano F (2002) Iterative image deformation methods in PIV. *Meas Sci Technol* 13:R1–R19. <https://doi.org/10.1088/0957-0233/13/1/201>
- Scully MP (1975) Computation of helicopter rotor wake geometry and its influence on rotor harmonic airloads (Ph.D. thesis). Massachusetts Institute of Technology
- Shtork SI, Vieira NF, Fernandes EC (2008) On the identification of helical instabilities in a reacting swirling flow. *Fuel* 87:2314–2321. <https://doi.org/10.1016/j.fuel.2007.10.016>
- Sieber M, Oliver Paschereit C, Oberleithner K (2016a) Advanced identification of coherent structures in swirl-stabilized combustors. *J Eng Gas Turbines Power* 139:021503. <https://doi.org/10.1115/1.4034261>
- Sieber M, Paschereit CO, Oberleithner K (2016b) Spectral proper orthogonal decomposition. *J Fluid Mech* 792:798–828. <https://doi.org/10.1017/jfm.2016.103>
- Sirovich L (1987) Turbulence and the dynamics of coherent structures. I. Coherent structures. *Q Appl Math* 45:561–571
- Skripkin S, Tsoy M, Shtork S, Hanjalić K (2016) Comparative analysis of twin vortex ropes in laboratory models of two hydro-turbine draft-tubes. *J Hydraul Res* 54:450–460. <https://doi.org/10.1080/00221686.2016.1168325>
- Smith TE, Douglas CM, Emerson BL, Lieuwen TC (2018) Axial evolution of forced helical flame and flow disturbances. *J Fluid Mech* 844:323–356. <https://doi.org/10.1017/jfm.2018.151>
- Steinberg AM, Boxx I, Stöhr M, Carter CD, Meier W (2010) Flow–flame interactions causing acoustically coupled heat release fluctuations in a thermo-acoustically unstable gas turbine model combustor. *Combust Flame* 157:2250–2266. <https://doi.org/10.1016/j.combustflame.2010.07.011>
- Stöhr M, Sadanandan R, Meier W (2011) Phase-resolved characterization of vortex–flame interaction in a turbulent swirl flame. *Exp Fluids* 51:1153–1167. <https://doi.org/10.1007/s00348-011-1134-y>
- Stöhr M, Boxx I, Carter CD, Meier W (2012) Experimental study of vortex–flame interaction in a gas turbine model combustor. *Combust Flame* 159:2636–2649. <https://doi.org/10.1016/j.combustflame.2012.03.020>
- Stöhr M, Arndt CM, Meier W (2015) Transient effects of fuel–air mixing in a partially-premixed turbulent swirl flame. *Proc Combust Inst* 35:3327–3335. <https://doi.org/10.1016/j.proci.2014.06.095>
- Stöhr M, Oberleithner K, Sieber M, Yin Z, Meier W (2017a) Experimental study of transient mechanisms of bistable flame shape transitions in a swirl combustor. *J Eng Gas Turbines Power* 140:011503. <https://doi.org/10.1115/1.4037724>
- Stöhr M, Yin Z, Meier W (2017b) Interaction between velocity fluctuations and equivalence ratio fluctuations during thermoacoustic oscillations in a partially premixed swirl combustor. *Proc Combust Inst* 36:3907–3915. <https://doi.org/10.1016/j.proci.2016.06.084>
- Syred N (2006) A review of oscillation mechanisms and the role of the precessing vortex core (PVC) in swirl combustion systems. *Prog Energy Combust Sci* 32:93–161. <https://doi.org/10.1016/j.pecs.2005.10.002>
- Towne A, Schmidt OT, Colonius T (2018) Spectral proper orthogonal decomposition and its relationship to dynamic mode decomposition and resolvent analysis. *J Fluid Mech* 847:821–867. <https://doi.org/10.1017/jfm.2018.283>
- Valera-Medina A, Syred N, Griffiths A (2009) Visualisation of iso-thermal large coherent structures in a swirl burner. *Combust Flame* 156:1723–1734. <https://doi.org/10.1016/j.combustflame.2009.06.014>
- Vanierschot M, Van Dyck K, Sas P, Van den Bulck E (2014) Symmetry breaking and vortex precession in low-swirling annular jets. *Phys Fluids* 26:105110. <https://doi.org/10.1063/1.4898347>

- Widmann A, Tropea C (2017) Reynolds number influence on the formation of vortical structures on a pitching flat plate. *Interface Focus* 7:20160079. <https://doi.org/10.1098/rsfs.2016.0079>
- Wunenburger R, Andreotti B, Petitjeans P (1999) Influence of precession on velocity measurements in a strong laboratory vortex. *Exp Fluids* 27:181–188. <https://doi.org/10.1007/s003480050343>
- Yazdabadi PA, Griffiths AJ, Syred N (1994) Characterization of the PVC phenomena in the exhaust of a cyclone dust separator. *Exp Fluids* 17:84–95. <https://doi.org/10.1007/BF02412807>
- Zakharov DL, Krasheninnikov SYu, Maslov VP, Mironov AK, Toktaliev PD (2014) Investigation of unsteady processes, flow properties, and tonal acoustic radiation of a swirling jet. *Fluid Dyn* 1:51–62. <https://doi.org/10.1134/S0015462814010086>
- Zhang R, Boxx I, Meier W, Slabaugh CD (2019) Coupled interactions of a helical precessing vortex core and the central recirculation bubble in a swirl flame at elevated power density. *Combust Flame* 202:119–131. <https://doi.org/10.1016/j.combustflame.2018.12.035>

**Publisher's Note** Springer Nature remains neutral with regard to jurisdictional claims in published maps and institutional affiliations.